

Influence of Cr and Y Addition on Microstructure, Mechanical Properties, and Corrosion Resistance of SPSed Fe-Based Alloys



V.M. SUNTHARAVEL MUTHAIAH and SUHRIT MULA

Present work investigates the microstructural stability during spark plasma sintering (SPS) of Fe-Cr-Y alloys, its mechanical properties and corrosion behavior for its possible applications in nuclear power plant and petrochemical industries. The SPS was carried out for the Fe-7Cr-1Y and Fe-15Cr-1Y alloys at 800 °C, 900 °C, and 1000 °C due to their superior thermal stability as reported in Muthaiah *et al.* [Mater Charact 114:43–53, 2016]. Microstructural analysis through TEM and electron back scattered diffraction confirmed that the grain sizes of the sintered samples depicted a dual size grain distribution with >50 pct grains within a range of 200 nm and remaining grains in the range 200 nm to 2 μm. The best combination of hardness, wear resistance, and corrosion behavior was achieved for the samples sintered at 1000 °C. The high hardness (9.6 GPa), minimum coefficient of friction (0.25), and extremely low wear volume ($0.00277 \times 10^{-2} \text{ mm}^3$) and low corrosion rate (3.43 mpy) are discussed in the light of solid solution strengthening, grain size strengthening, grain boundary segregation, excellent densification due to diffusion bonding, and precipitation hardening due to uniformly distributed nanosize Fe₁₇Y₂ phase in the alloy matrix. The SEM analysis of the worn surface and corroded features corroborated well with the wear resistance and corrosion behavior of the corresponding samples.

<https://doi.org/10.1007/s11661-017-4448-4>

© The Minerals, Metals & Materials Society and ASM International 2017

I. INTRODUCTION

FE-CR based alloys are extensively useful in many applications including nuclear power plants, petrochemical industries, hot acid container, heat exchanger and construction industry^[1,2] due to their attractive corrosion, wear and oxidation resistance and appreciable mechanical strength as well as good formability.^[3–5] The yield strength and other mechanical properties increase significantly due to the grain size reduction (to ultrafine range) as per the Hall–Petch relationship.^[6,7] Bulk metals and alloys with nanocrystalline/ultrafine grains could be produced by various severe plastic deformation (SPD) techniques such as cryorolling, ECAP, ARB, multi-axial forging, and high pressure torsion.^[8] But, for immiscible alloy systems, such as Fe-Cr-Y, the SPD techniques cannot be useful to produce homogeneous nanocrystalline solid solutions/alloys. Therefore, non-equilibrium processing routes must be followed to

prepare such alloys. Among the non-equilibrium routes, mechanical alloying (MA) followed by consolidation using spark plasma sintering (SPS) seems to be an efficient method in producing such ultrafine grained/nanocrystalline structures.^[9,10] Among the other non-equilibrium processes, the MA is preferred due to its effectiveness in preparing highly supersaturated solid solutions easily in large quantities.^[10] Although, the SPS technique primarily was developed for producing bulk ceramic materials, recently many researchers have reported that it is possible to produce bulk nanostructured metallic materials such as Cu,^[11] Ni,^[12] Al^[13], and Fe-based alloys through SPS.^[14,15]

The major challenge in processing such nanostructured material is to obtain fully dense bulk size components retaining its nanocrystalline features. Groza^[16] reported to compact nanocrystalline materials by many techniques including hot pressing (HP)/hot isostatic pressing (HIP) and explosive compaction. The compaction of nanocrystalline Fe-Cr alloys is very difficult due to their body-centered cubic structure and associated high hardness values which require a very high compaction pressure and high temperature for consolidation. Gupta *et al.*^[5] reported that the annealing treatment of the ball-milled nanocrystalline Fe-10 wt pct Cr alloy was helpful for densification by conventional pressing using a pressure of 2.7 GPa. The

V.M. SUNTHARAVEL MUTHAIAH and SUHRIT MULA are with the Metallurgical and Materials Engineering Department, Indian Institute of Technology, Roorkee, Roorkee 247667, India. Contact e-mail: smulafmt@iitr.ac.in

Manuscript submitted June 10, 2017.

Article published online December 24, 2017

high hardness value of ~ 10 GPa was reported for pure nanocrystalline iron (grain size 10 nm).^[17] It is reported that at least a pressure of $\geq 1/3$ rd of the hardness (*i.e.*, 3.5 GPa) of the material is essential for proper compaction.^[17] Moreover, consolidation at high temperatures, the material loses their nanocrystalline structures leading to produce microcrystalline grains. Therefore, in order to optimize the compaction process, more advanced techniques should be utilized. Toor *et al.*^[15] reported that the SPS of ball-milled Fe-18Cr-2Si sample (at 1100 °C with a heating rate of 50 °C/min at a constant pressure of 60 MPa), showed the maximum densification of ~ 96.0 pct, which resulted in a hardness of 710 HV corresponding to the minimum grain size of 20 to 40 nm. Sorour *et al.*^[4] investigated the SPS characteristics of the ball-milled Fe-Cr-B alloy. They reported a ~ 97 pct densification of the alloy when sintered at 1150 °C with an applied pressure of 50 MPa and found a very high hardness of 9.7 GPa. Further, Shongwe *et al.*^[18] examined the SPS characteristics of the conventional grained Fe-30 pct Ni mixture sintered at 1230 °C with an applied pressure of 30 MPa. They reported an average grain size of 200 μm with 98.7 pct sintered density, and the corresponding microhardness value was 284 HV. They also found that the fracture morphology shifted from purely intergranular type to a transgranular fracture when the sintering temperature increased to 1230 °C from 950 °C. Sebayagan *et al.*^[19] investigated the sintering behavior of the ball-milled Fe-20 wt pct Cr samples consolidated by SPS and HP. The SPS was carried out at 800 °C and 900 °C with a heating rate of 400 °C/min using a pressure of 120 MPa, whereas the HP was done using a steel die-punch at a pressure of 25 MPa at 1000 °C. The SPS was reported to be more effective in retaining the nanocrystalline grain structure as compared to that by the HP [*e.g.*, 18 nm for spark plasma sintered (SPSed) as compared to 39 nm of the HPed sample] and found to have better mechanical properties (hardness of 8.31 GPa for the SPSed sample in contrast to 4.94 GPa for HPed sample). The major advantage of the SPS over HP/HIP is simultaneous compaction of the nanocrystalline powder particles along with sintering/bonding to produce a highly dense bulk structure at a relatively low temperature with a less sintering time (typically a few minutes),^[9] which helps to retain the ultrafine/nanocrystalline features. The important challenges during the SPS are to achieve full densification of the nanometric metallic powders without causing any significant grain growth in order to obtain ultrafine/nanocrystalline structure. The pulsed electrical current with a DC bias voltage in SPS can produce highly dense nanocrystalline structure, if the sintering parameters are effectively synchronized.

The SPS characteristics of the ball-milled Fe-Cr-Y nanocrystalline disordered solid solutions and their mechanical properties have not yet been reported. The Fe-Cr-Y nanocrystalline alloys were first developed by MA and then on the basis of their thermal stability, the SPS process has been optimized (temperature, dwell time and pressure) to achieve nearly full dense compacts. Effect of sintering temperature has been evaluated and

explained in the light of microstructural evolution, densification, microhardness variation, wear resistance, and corrosion behavior.

II. EXPERIMENTAL DETAILS

A. Materials and Method

MA was carried out to synthesize Fe-7Cr-1Y and Fe-15Cr-1Y (all in at. pct) alloys to investigate SPS characteristics and its effect on mechanical properties, wear resistance, and corrosion behavior. Elemental powder blends of iron (Fe), chromium (Cr), and yttrium (Y) (purity >99.0 pct and particle size of 20 to 100 μm , Alpha Aesar) were mechanically alloyed in hardened steel grinding media with stainless steel balls (17 in numbers of 8 mm diameter and 16 in numbers of 6 mm diameter) using SPEX 8000M shaker mill. The milling was carried out for 25 hours at room temperature to achieve supersaturated disordered alloys and powder-to-ball weight ratio was kept at 1:10 throughout the milling operation. In order to maintain inertness, the vial was sealed inside the glove box filled with high-purity argon atmosphere prior to milling. Chemical analysis of the as-milled Fe-15Cr-1Y sample was carried out by X-ray photoelectron spectroscopy (PHI 5000 versa probe III). Peaks were fitted and analyzed by using Multipak software. Surface composition and concentrations were calculated from appropriate peak area.

B. Spark Plasma Sintering (SPS)

The as-milled powder samples of the Fe-7Cr-1Y and Fe-15Cr-1Y compositions were spilled into the graphite die and punch with 10 mm diameter. SPS was carried out at 800 °C, 900 °C, and 1000 °C under high-purity argon atmosphere using Dr. Sinter 625 machine. The heating rate was maintained at 100 °C/min and holding time was kept for 5 minutes at each sintering temperature. The pressure was maintained at 60 MPa (≈ 4.7 kN) throughout the sintering process. The sintering temperature was monitored through real-time measurement by a K-type thermocouple which is fixed permanently in the SPS machine.

C. Microstructural Analysis

Phase analysis of the as-milled and SPSed samples was carried out by using X-ray diffraction (XRD) analysis. The XRD analysis was done in Rigaku smart Lab X-ray diffractometer using Cu $K\alpha$ radiation. X'pert high score plus software was used to strip off the Cu $K\alpha_2$ contribution to the peaks and for background subtraction. The three major XRD peaks were used to determine the average crystallite size by removing the broadening caused by the lattice strain and thereby using the plots of $B_r \cos\theta$ vs $\sin\theta$.^[20,21] The density of the SPSed samples was calculated by Archimedes principle using a density measuring kit (Mettler Toledo AG). The microstructural studies of the sintered samples were carried out using an optical microscope

(DM15000MTM Leica, Switzerland), field emission scanning electron microscope (Model Zeiss 51-ADD0048), and transmission electron microscope (JEOL 2000FX). Based on the XRD crystallite size, relative density, and microhardness values of the SPSed (1000 °C) samples, detailed microstructural features were investigated by electron back scattered diffraction (EBSD). The EBSD analysis was performed using FEI-Quanta 200 FE-SEM equipped with the TSL data acquisition system. For the EBSD analysis, the sintered sample was first mechanically polished on fine cloth using colloidal silica. Then, the sample was electropolished in an electrolyte of 20 pct perchloric acid in methanol at -40 °C and the electropolishing system was operated at 21 V for 50 seconds. The EBSD scan was performed on the polished sample with a step size of 0.05 μm and subsequently analyzed by TSL-OIM software. Vickers microhardness measurements were performed on the surface of the SPSed samples with a load of 50 g, which prevented indentation along the particle boundaries. The particle diameter-to-indent depth ratio was fixed at 10:1 to carry out the hardness tests. Each reported microhardness value is the average of 10 such measurements, which is shown as statistical deviation for each data. Based on the XRD crystallite size, relative density, and microhardness values, detailed microstructural features of the SPSed (1000 °C) samples were analyzed by using TEM. The TEM samples were initially mechanically polished with different grades of SiC abrasive papers to thin down to <100 μm . Further, the sintered samples were electropolished by a twin-jet electropolishing equipment (function at 30 to 40 V) using a solution of 95 pct methanol + 5 pct perchloric acid at room temperature. Detailed investigation of the TEM samples was performed using JEOL 2000FX function at 200 keV which was linked to digital micrograph software.

D. Corrosion Test

Corrosion behavior of the nanocrystalline SPSed specimens of the Fe-7Cr-1Y and Fe-15Cr-1Y compositions was carried out through potentiodynamic polarization tests. The study was performed at room temperature using an aerated 3.5 wt pct aqueous sodium chloride solution. The specimens were polished using different grades of SiC abrasive papers (100, 300, 800, 1000, 1200, 1500, and 2000) followed by cloth polishing using alumina powder (0.02 μm) emulsion. A graphite rod and a saturated calomel electrode (SCE) were used as the auxiliary electrode and reference electrode, respectively. Moreover, the sintered specimen functioned as the working electrode. The electrodes were kept in a flat cell such that an area of 1 cm^2 of the sintered specimen was exposed to the test solution. A ratio between solution volume to specimen surface area was maintained at 300 mL/cm^2 . Prior to the polarization test, the specimens were stabilized for duration of 110 minutes. During this period, the variation in the open circuit potential was recorded as a function of time. The polarization investigations were carried out at a scan rate of 100 mV/min from -250 to $+500$ mV in

the cathodic and anodic directions, respectively. Tafel extrapolation method was used to calculate the corrosion current density (i_{corr}) and corrosion potential (E_{corr}) from the polarization curves. After the polarization test, nature of the corrosion attack of the sintered samples was determined through FE-SEM image analysis.

E. Wear Test

The dry sliding wear test of the sintered samples was performed on a ball-on-disk type tribometer (TR-201E-M2, DUCOM, Bangalore, India). The dimension of the cylindrical sample was 10 mm in diameter and 2 mm in thickness. Acetone was used to clean the surface of the sintered samples. A single crystal spherical alumina ball with a diameter of 10 mm was used as a counter-body. The hardness of the counter-body is ~ 2000 HV. The sample, which was fixed with circular stainless steel plate, was rotated against the stationary Al_2O_3 ball fixed with the machine. The applied load was maintained at a constant value of 20 N and the rotational speed (0.01 m/s) was kept constant at 500 rpm. The wear experiments were carried out at an ambient condition (at room temperature) in open air for 25 minutes. The ratio of the frictional force to the normal load (*i.e.*, 20 N) was used to determine the coefficient of friction (COF). At real time, the COF was generated using an electronic sensor which automatically recorded the frictional force induced between the Al_2O_3 ball and the sintered sample. The surface profile of the worn specimens was analyzed with the help of profilometer (SJ 400, Mitutoyo, Japan) through the measurements of width and depth of the wear scars. For each type of sample, minimum 3 wear tracks and 10 such measurements per track were examined to obtain the average value of the width and wear depth of the wear scar. Subsequently, the worn surfaces were examined using FE-SEM to characterize the wear mechanisms.

III. RESULTS AND DISCUSSION

A. Microstructure of the As-milled and SPSed Samples

Figures 1(a) and (b), respectively, show the XRD analysis of the Fe-7Cr-1Y and Fe-15Cr-1Y alloys both in the as-milled and SPSed conditions. It can be observed that the Cr and Y peaks are not visible in the as-milled samples of both the alloys. Therefore, as per the XRD patterns, it can be observed that the complete solid solution is formed after MA for 25 hours. The complete solid solution formation of the Fe-Cr-Y alloys and their thermal stability have been discussed in detail in our previous work published in Reference 22. Chemical analysis was carried out for the as-milled sample of the Fe-15Cr-1Y alloy to confirm whether any oxygen pick-up was there in the as-milled sample. The chemical composition of the milled powder is found to be Fe: 84.1 pct, Cr: 14.55 pct, Y: 0.95 pct, and O: 0.4 pct (all in at. pct), which shows a bit amount of oxygen picked up by the material from the milling

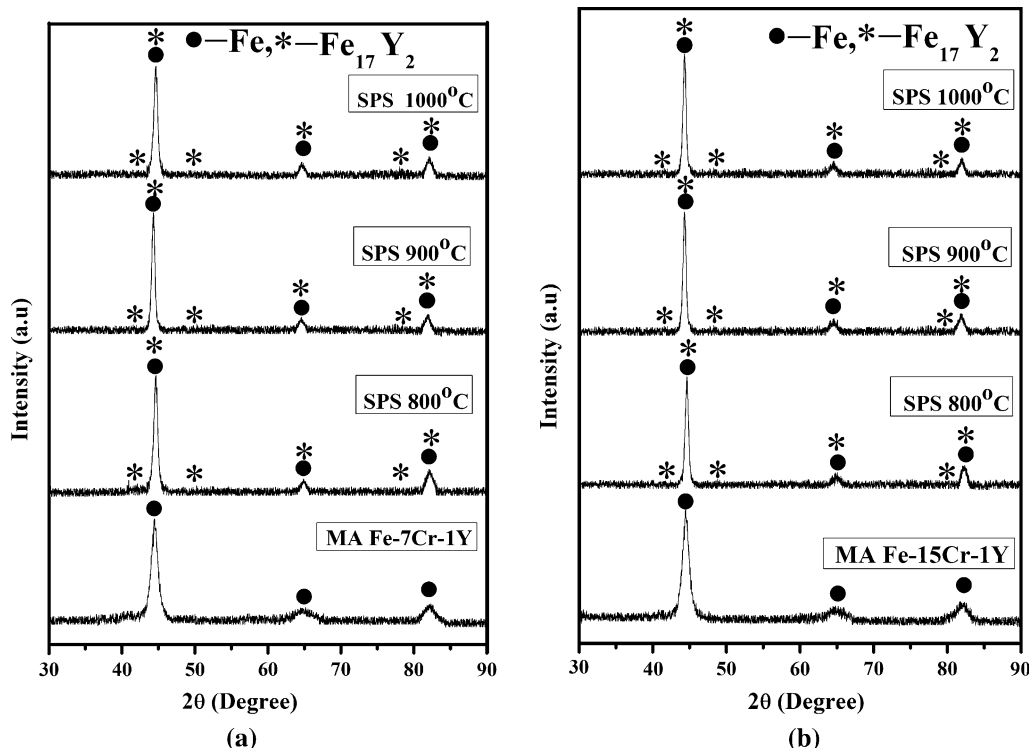


Fig. 1—XRD patterns of the as-milled and SPSed samples of (a) Fe-7Cr-1Y and (b) Fe-15Cr-1Y alloys sintered at various temperatures.

media and/or during material handling. The trace amount of oxygen picked up was possibly due to the Y atoms because of its high affinity to oxygen, which is also suggested by other researchers.^[23,24] But, the oxide formation of Y was not possible to detect by the XRD phase analysis because of its limitation of the detectability (at least 2 wt pct should be present).^[20,21] The formation of yttrium oxide could play a pivotal role to improve the thermal stability of the milled alloy through Zener pinning.^[23,24] Increase in the thermal stability of Fe-based alloys due to formation of small amount of oxides was also reported by other researcher.^[23,24] The formation of HfO₂ nanoparticles (average size ~4 nm) during annealing (at 900 °C for 1 hours) of Fe-14 at. pct Cr-4 at. pct Hf alloy reported to increase its thermal stability. The thermal stability also increased due to the formation of other second-phase particles such as HfC, M₂₃C₆ and Fe-Cr-Hf intermetallic. The nanosize particles dispersed throughout the ferritic matrix could provide effective kinetic pinning to stabilize nanocrystalline grain structure.^[24] Xu *et al.* reported the formation of ZrO₂ nanoparticles during subsequent annealing of the Fe-14 at. pct Cr-1.5 at. pct Zr alloy, instead of forming the oxide during MA.^[25] The formation of ZrO₂ nanoparticles during annealing suggested that the milled nanocrystalline powder adsorbed oxygen (~0.2 wt pct) because of the high affinity of Zr to oxygen ($\Delta G_f = -1037$ kJ/mol). They also reported that uniformly dispersed nanosize ZrO₂ particles (average size ~3.7 nm) rendered the Fe-based alloy powders to achieve high thermal stability (retained nanocrystalline structure even after annealing at 900 °C for 1 hour).^[25]

For both the compositions, the XRD phase analysis of the SPSed samples clearly shows the formation of Fe₁₇Y₂ intermetallic phase, which is correlated with the phase evolution of the annealed samples of the same composition.^[22] It can also be observed (especially from the lower angle peaks) that as compared to the as-milled samples, the peak intensity gradually increased and peak width (Fe 110 reflection) at FWHM decreased as a function of increase in the sintering temperature. Further, the decrease in the peak width and increase in the peak intensity could be ascribed to the increase in the crystallite size and release of the accumulated lattice strain, which decreased net dislocation density. Saenko *et al.* reported experimental and calculated enthalpies for the formation of Fe₁₇Y₂ (-1.78 to -8.7 kJ/mol/at) phase at a temperature range from 0 to 298 K.^[26] They mentioned that Fe₁₇Y₂ and Fe₂₃Y₆ compounds were unstable at 0 K based on the results of *ab initio* calculations as per Mihalkovic and Widom model.^[27] Additionally, no experimental data are available about any phase transformation in the Fe-Y binary system at low temperatures.^[26] Based on the experimental results of heat capacity measurement by Mandal *et al.*,^[28] the standard entropy of Fe₁₇Y₂ compound at 298.15 K is found to be 34.5 J/K/mol. Rybalka analyzed the kinetic model for the H₂-induced direct phase transformation of Fe₁₇Y₂. The author reported that effective activation energy (*Q*) for the same (*i.e.*, formation of Fe₁₇Y₂) varying from 162 to 242 kJ/mol as the temperature varies from 330 °C to 750 °C. The author also correlated that there was a good agreement with the *Q* for diffusion of Fe atoms in rare-earth metals (250 kJ/mol) and self-diffusion of Fe in α -Fe (250.6 kJ/mol).^[29]

In an ODS alloy (Fe-Cr containing Ti and Y_2O_3), it was reported that the formation of Y-Ti-O (e.g., $Y_2Ti_2O_7$) oxides at room temperature requires an enthalpy of -3874 kJ/mol as reported by Pasebani and Charit.^[30] The formation of Cr-Y-Ti-O nanoclusters was explained through the mechanism of concentration and diffusion rates of the initial oxide species formed during the milling process. Further, initial stages of sintering as well as the thermodynamic nucleation barrier and their enthalpy of formation also played pivotal roles in the formation of nanocluster oxides. Schneibel and Shim^[31] investigated the internal oxidation of $Fe_{17}Y_2$ and $Fe_{11}TiY$ intermetallic phases to produce ODS alloys containing 30 pct of oxide particles (Y_2O_3 , $YFeO_3$, $Y_2Ti_2O_7$, and Fe_2TiO_4) distributed in a Fe-based solid solution matrix. The ODS alloy showed a good thermal stability up to 600 °C with oxides particles of ~ 20 nm size; thereafter, substantial coarsening of the oxides was reported. The coarsening of the oxides particles was ascertained to the high volume fraction of dispersoids, which caused faster coarsening due to short diffusion distance and short particle–particle distance. The presence of impurities segregated at the dispersoid–matrix interfaces also could play important role in faster coarsening.^[31]

Variation of crystallite size vs sintering temperature is shown in Figure 2. The three major XRD peaks were used to determine the average crystallite size by using Williamson–Hall analysis.^[20,21] The effect of peak broadening caused by the lattice strain was removed by using the plot of $B_c \cos \theta$ vs $\sin \theta$. The peak broadening was evaluated by measuring the width of the peak at intensity equal to half of the maximum intensity (FWHM). The average crystallite size is determined to be ~ 53 and 33 nm, respectively, for the Fe-7Cr-1Y and Fe-15Cr-1Y samples, which were sintered at 800 °C. Further, the crystallite size increased to 72 and 60 nm, respectively, when the sintering temperature was raised to 1000 °C. Moreover, coarsening of the crystallite size is found to be sluggish in case of the Fe-15Cr-1Y samples as compared to the Fe-7Cr-1Y samples. It could be noticed that when a large amount of Cr is dissolved in the presence of Y, the solid solution strengthening is more effective to stabilize it. Overall for both the compositions, the average crystallite size is found to remain well within 100 nm even after sintering at 1000 °C. The major role of Cr in the nanocrystalline Fe was only to enhance the strengthening to the matrix and not for the grain size stabilization.^[32–34] The average crystallite size of the as-milled Fe-7Cr-1Y and Fe-15Cr-1Y alloys was found to be 9 and 7.5 nm, respectively, and the same samples showed 16 and 15 nm crystallite size after annealing at 600 °C. Without any Y, the Fe-15Cr showed a crystallite size of 128 nm when annealed at 1000 °C.^[22] It can be noticed that Cr could play a pivotal role in grain size stabilization in the presence of 1 at. pct Y up to certain temperature (i.e., 600 °C). Thereafter above 600 °C, it clearly showed a tendency to grain coarsening but retaining the grain size within 100 nm even after annealing at 1000 °C. The growth rate of the crystallite size at higher temperatures is found to be bit higher for the high Cr content alloy

(i.e., Fe-15Cr-1Y). This may be due to the weak stabilizing effect of Cr in Fe-based alloys as also suggested by various researchers.^[32–34] Darling *et al.* investigated that the solute atom of Cr and Ni are poor candidates for the thermodynamic stabilization of nanocrystalline Fe, whereas the nanocrystalline Fe was strongly stabilized by Zr.^[32] Saber *et al.* reported that the crystallite size of Fe-10 at. pct Cr and Fe-18 at. pct Cr was estimated to be 80 and 70 nm, respectively, after annealing at 600 °C. Thereafter, the grain growth took place. For example, the grain size was found to be 7 μ m for the Fe-10 at. pct Cr alloy after annealing at 900 °C. They also reported that the addition of 4 at. pct Zr to the Fe-10 pct Cr and Fe-18 pct Cr stabilized the grains at <100 nm after annealing at 1000 °C.^[33] Li *et al.* also reported that addition of 4 at. pct Hf to the Fe-14Cr alloy stabilized the grain size at less than 100 nm after annealing at 1000 °C, whereas the Fe-14Cr alloy without Hf addition showed the grain size ~ 140 nm when the sample was annealed at 600 °C.^[34] Therefore, overall, it can be concluded that Cr could enhance the thermal stability in the presence of oversize solute atoms such as Zr and Y. This is also observed in the present study.

The variation of the lattice parameter is displayed in Figure 3. The lattice parameter (a_{Fe}) of the Fe-15Cr-1Y as-milled sample is found to be 2.909 Å as compared to 2.892 Å for the Fe-7Cr-1Y in the same condition as reported in our previous study.^[22] The a_{Fe} of the alloys sintered at 800 °C is determined to be 2.874 and 2.888 Å, respectively. The a_{Fe} of the sintered samples found to decrease with increase in the sintering temperature and the trend is similar for the both alloys. The a_{Fe} was found to be 2.868 and 2.881 Å, respectively, after sintering at 1000 °C. The reduction in the lattice parameter is found to be prominent with an increase in the sintering temperature. This could be attributed to the two reasons: (i) the excess solute atoms, especially oversize Y atoms (Cr has little role as it has spontaneous solid solubility in Fe) could have precipitated out of the solid solution to segregate along the grain boundary areas and/or (ii) the formation of intermetallic compound(s) such as $Fe_{17}Y_2$ at high temperature. In the present study, formation of the $Fe_{17}Y_2$ phase already been detected and definitely, the a_{Fe}

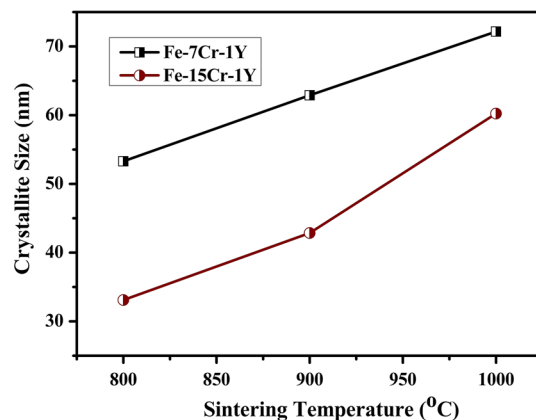


Fig. 2—Variation of crystallite size as a function of sintering temperatures for the Fe-7Cr-1Y and Fe-15Cr-1Y alloys.

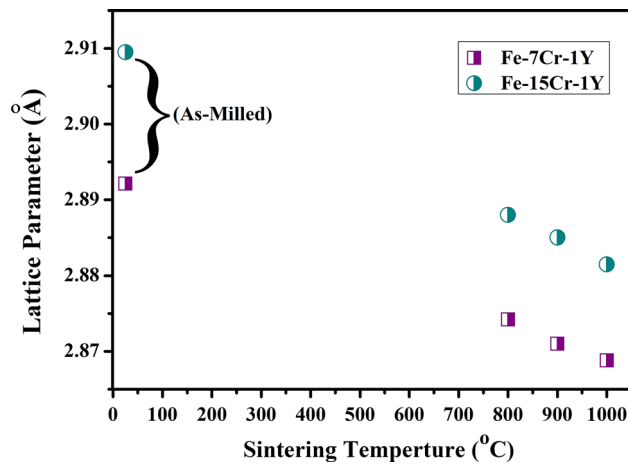


Fig. 3—Variation of the lattice parameter of the Fe-7Cr-1Y and Fe-15Cr-1Y alloys. SPSed at various temperatures as compared to that of the as-milled samples.

decreased due to the formation of Fe_{17}Y_2 phase as Y atoms had to come out of the solid solution to form the intermetallic phase. It is to be noted that the amount of the alloying content (*i.e.*, Y), which is precipitated out of the solid solution to form Fe_{17}Y_2 intermetallic phase and/or segregated along the grain boundaries, played an important role in the decrease of the a_{Fe} of the Fe-based solid solution.^[35,36]

Figures 4(a) and (b), respectively, show typical temperature and displacement (mm/°C, dotted lines) profiles as a function of dwell time over the densification during SPS of the nanostructured Fe-7Cr-1Y and Fe-15Cr-1Y alloys. The sintering was carried out at 800 °C, 900 °C, and 1000 °C by applying a constant pressure of 60 MPa for a holding period of 5 minutes, while a heating rate of 100 °C/min was used to raise the sintering temperature. Figure 4 indicates that the relative sintering density achieved during the SPS at different sintering temperatures could easily be measured indirectly from the corresponding displacement profile (mm/°C). The densification of the alloy powders during SPS was monitored through the analysis of the displacement curves stimulated from the software (wave logger) installed with the SPS machine.^[18] The displacement of the specimen could be affected either by the pressure, time, and/or the temperature. Archimedes principle was used to determine the relative density of the sintered samples. The relative density was measured to be ~86 and 87 pct, respectively, for the Fe-7Cr-1Y and Fe-15Cr-1Y samples when the SPS was performed at 800 °C [Figure 4(c)]. It can be noticed that the sintered density increases with increasing sintering temperature and the maximum sintered density achieved is 96 and 97 pct, respectively, for the Fe-7Cr-1Y and Fe-15Cr-1Y samples, when sintered at 1000 °C. Figure 4(c) also indicates the level of porosity present in the respective sintered samples. The larger sintered density could be ascribed to the prevalent grain boundary diffusion at the higher sintering temperature, due to which the porosity level decreased to enhance proper bonding between the particles.

The SPS can develop highly dense bulk samples without much affecting the grain structures of various metals and ceramics due to its rapid heating rate, minimum holding time, and a comparatively lower sintering temperature.^[37] But, mechanisms of the SPS still remain imprecise. The DC current (on-off), which is used for simultaneous development of spark discharge and rapid heating (Joule effect) between the powder particles in the initial stage of the SPS, is generally reported to be responsible to achieve high sintered density in the SPS.^[9] Further, the pulse current developed removes the thin oxide layers of the metallic materials, surface impurities, and adsorbents induced by plasma generation and thus enhancement in the bonding between the powder particles is achieved.^[38] These special effects result in low heat input and create bonding between the powder particles with a limited chemical interaction among different elements and control grain sizes.^[18] In SPS, external pressure is applied not only to create electrical contacts between die, punch, and powder particles, but also progressively promotes densification by reorganization of the powder particles and neck formation through diffusion bonding due to localized deformation at the contact points.^[39] Nanostructured powders material densification may occur by some specific mechanisms such as plastic deformation, grain boundary sliding,^[40] grain growth, and grain rotation^[41] and even by grain boundary melting due to large Hertzian stress.^[42] Overall, all the factors together play their pivotal role to achieve such high level of densification.

The optical micrographs of the sintered specimens are shown in Figures 5(a) through (f). From the micrographs of the sintered samples, it can be observed that the amount of porosities decrease with increasing the sintering temperature. It can be observed from Figures 5(a) and (d), that the samples, which were sintered at 800 °C, have lot of porosities and the corresponding sintered density was found to be low for both the samples, *i.e.*, 86 pct (Fe-7Cr-1Y) and 87 pct (Fe-15Cr-1Y) only. The microstructures exhibited a few large and a lot of small porosities as a result of improper bonding and densification. Also, numerous free-standing particles, which do not exhibit any neck formation with the adjacent particles, could be observed from the micrographs of the samples sintered at 800 °C and 900 °C. This may be ascribed to the insufficient grain boundary diffusion at low sintering temperature with less dwell time (5 minutes). A significant enhancement in the relative sintered density was achieved when the samples were sintered at 1000 °C. The maximum sintered density of both the alloy samples is found to be 96 and 97 pct, respectively, when the SPS was done at 1000 °C. The corresponding porosity level also decreased to a very low level as could be observed from Figures 5(c) and (f). It can be noticed from Figures 5(a) through (f) that the grain size is not resolved clearly in any case. Therefore, higher magnification microscopy, such as TEM and EBSD are required to reveal the nanosize/ultrafine grains (discussed later in this section). The porosity level is found to be almost eliminated for the Fe-15Cr-1Y sample SPSed at 1000 °C, which can be

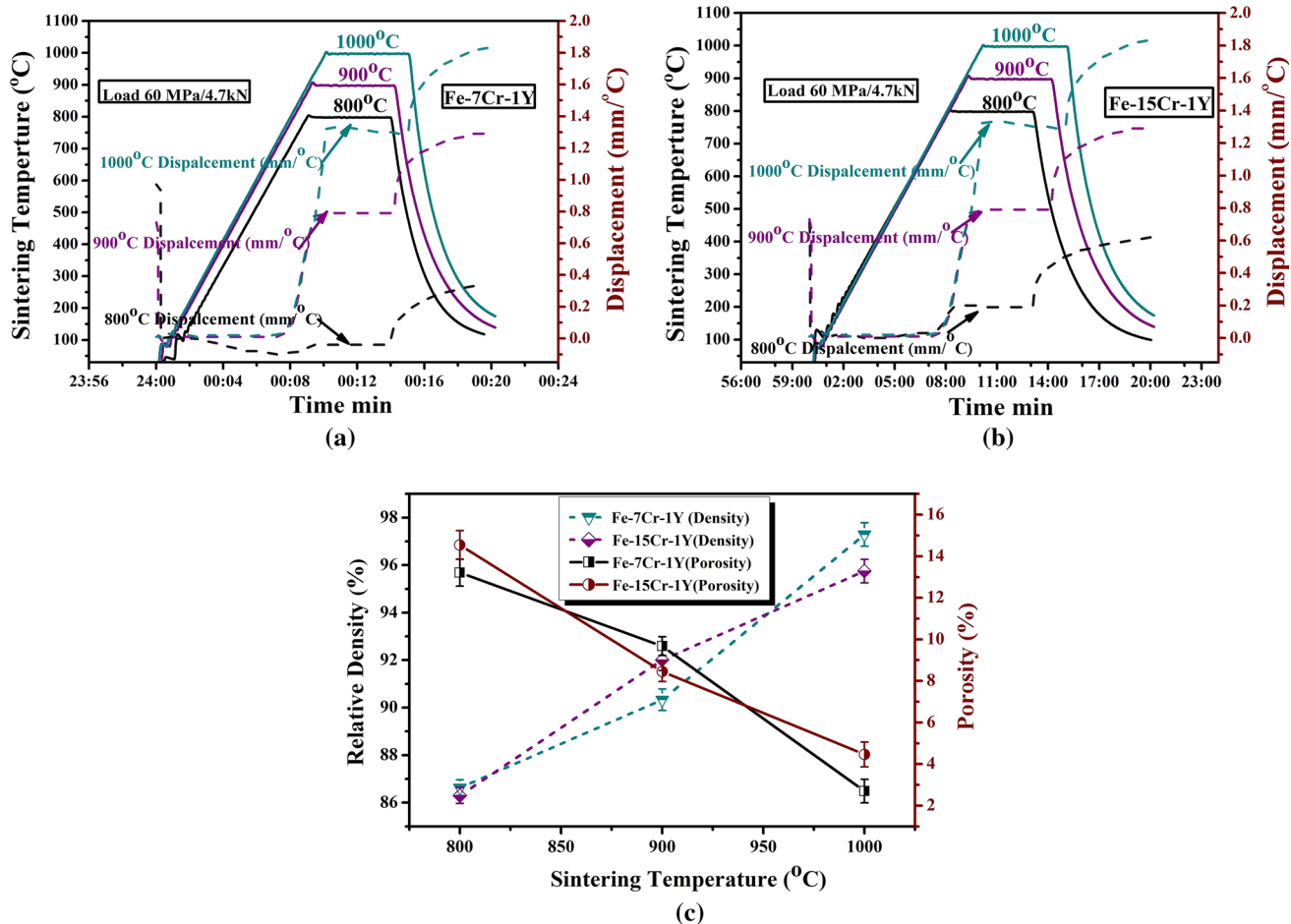


Fig. 4—Temperature profiles during SPS of (a) Fe-7Cr-1Y and (b) Fe-15Cr-1Y alloys at different temperatures. (c) Relative density and porosity as a function of sintering temperatures.

ascertained from the highly magnified image as shown in the inset of Figure 5(f) and a near-full density structure was developed.

Secondary electron (SE) and backscattered electron (BSE) images were recorded to reveal the level of porosity and densification clearly. Figures 6(a) through (f) show the SE as well as BSE images of each sample of the Fe-7Cr-1Y and Fe-15Cr-1Y alloys sintered at 800 °C, 900 °C, and 1000 °C. It can be noticed that the BSE mode is more prominent as compared to the SE mode to corroborate the sintered density. The BSE micrographs clearly revealed the presence of number of small pores in the low-temperature SPSed samples (800 °C and 900 °C). When the sintering temperature increased to 1000 °C, almost no porosity could be observed and achieved almost a near-full density samples for both the alloys. In some images, the presence of alumina (Al_2O_3) particles could be seen (encircled with red color, Color figure online), which are plausibly embedded during cloth polishing of the samples. Therefore, it can be concluded that the optical and SEM images of the SPSed samples revealed the surface morphology comprising larger and small size porosities. Further, it is corroborated well with the relative sintered density obtained by the Archimedes principle.

Figure 7(a) shows the variation of microhardness values of the Fe-7Cr-1Y and Fe-15Cr-1Y alloys as function of the sintering temperature. An important observation is that the microhardness value increased gradually with increase in the sintering temperature, and the maximum microhardness value for both the alloys (9.27 and 9.58 GPa, respectively) was obtained after sintering at 1000 °C. Further, the highest hardness of the sintered samples is found to be less as compared to that of the as-milled samples. It is to be noted that the microhardness value for the as-milled Fe-7Cr-1Y and Fe-15Cr-1Y alloys was determined to be 10.2 and 10.4 GPa, respectively. The average crystallite size of the as-milled Fe-7Cr-1Y and Fe-15Cr-1Y samples was estimated to be ~9 and 7.5 nm, respectively.^[22] It could be observed from Figure 2 that the average crystallite size of the Fe-7Cr-1Y and Fe-15Cr-1Y alloys sintered at 1000 °C was found to be 72 and 60 nm. Overall, the crystallite size and microhardness values gradually increased with an increase in the sintering temperature. In general, this is contradictory: an increase in the crystallite size would decrease the hardness value. Hence, the increase in the hardness value due to the densification overcompensates the decrease in the hardness because of the grain coarsening. Hence, the

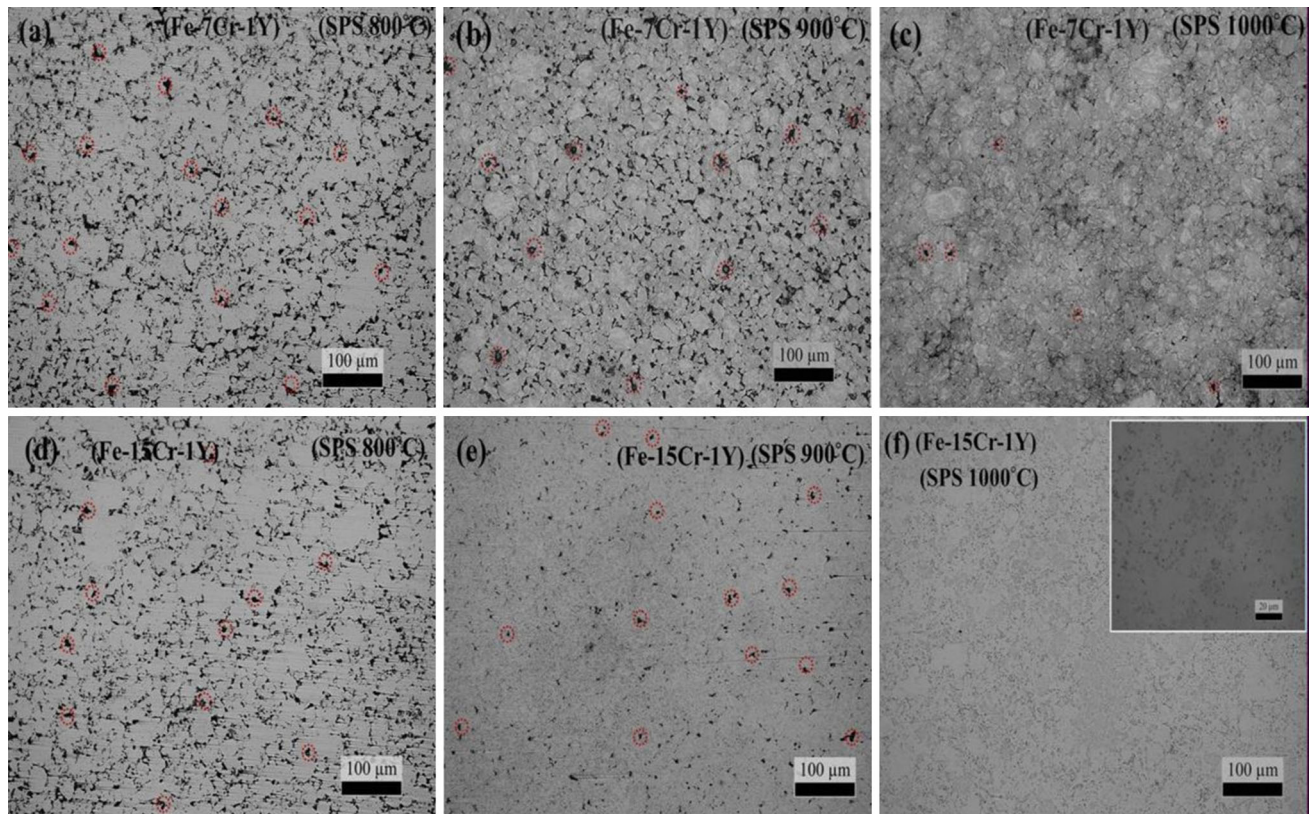


Fig. 5—Optical micrographs of bulk samples sintered at (a) 800 °C, (b) 900 °C, (c) 1000 °C for the Fe-7Cr-1Y composition; and (d) 800 °C, (e) 900 °C, (f) 1000 °C for the Fe-15Cr-1Y composition.

enhancement in the hardness value at higher sintering temperature can be accomplished mainly by two factors, *viz.* (i) an increase in the sintered density at elevated sintering temperature and (ii) formation of the harder intermetallic phase, *i.e.*, Fe_{17}Y_2 uniformly distributed within the matrix [Figures 1(a) and (b)]. It can be noted that the maximum hardness of the sintered samples is less than that of the as-milled samples. This can be ascribed mainly to the coarsening of grains and the presence of bit porosity (96 and 97 pct densification) of the sintered samples. The hardness measurement of the sintered samples was done randomly on the polished surface, which may include the influence of small pores, whereas the indentation on the as-milled samples was made within the larger size particles. Figure 7(b) shows the indentation marks made on the surface of the sintered samples during microhardness measurements. The particle diameter-to-indenter depth ratio was kept at 10:1 to avoid the effect of indentation plastic zone during the hardness tests. Further, the distance between the indentations was fixed at 1:3 for the hardness measurements. Each reported value of the hardness is an average of 10 such measurements. Zhang *et al.*^[43] also reported that the average microhardness value increased due to increase in the sintered density of the Fe-0.8 pct C steel sintered at higher temperature although the crystallite size increased with sintering temperature. Hussein *et al.*^[44] reported that the hardness value of the Nb-Zr alloys increased significantly due to the

enhanced sintered density at higher sintering temperatures.

Bright-field TEM images along with corresponding SAED pattern of the Fe-15Cr-1Y alloy sintered at 1000 °C are shown in Figures 8(a) through (c). Figures 8(a) and (b) clearly show that the grain sizes are varying from nanometer to ultrafine range (*i.e.*, a bimodal grain structure). The bright-field TEM images clearly show that the grain sizes are retained well within the ultrafine range (along with some nanocrystalline grains) even after the SPS at 1000 °C. The SAED pattern was recorded from the region as shown in Figure 8(a). As shown in Figure 8(c), the corresponding SAED pattern shows continuous rings along with some brighter spots indicating the presence of nanocrystalline features along with some larger size grains in the microstructure. As indicated in Figure 8(c), the rings are identified as the major reflections from the Fe (110), (220), (200) planes along with the reflections from the hcp intermetallic phase, Fe_{17}Y_2 (222), Fe_{17}Y_2 (600), and Fe_{17}Y_2 (302). The presence of the hcp intermetallic Fe_{17}Y_2 phase was also detected from the XRD phase analysis of the sintered sample [Figure 1(b)]. Neither, the SAED nor the XRD pattern exhibited the presence of any free Cr and Y elements. This indicates the dissolution of the added Cr and Y in the formation of the disordered solid solution of Fe during MA, and Y partially transformed to Fe_{17}Y_2 intermetallic phase during the SPS process. Formation of the Fe_{17}Y_2

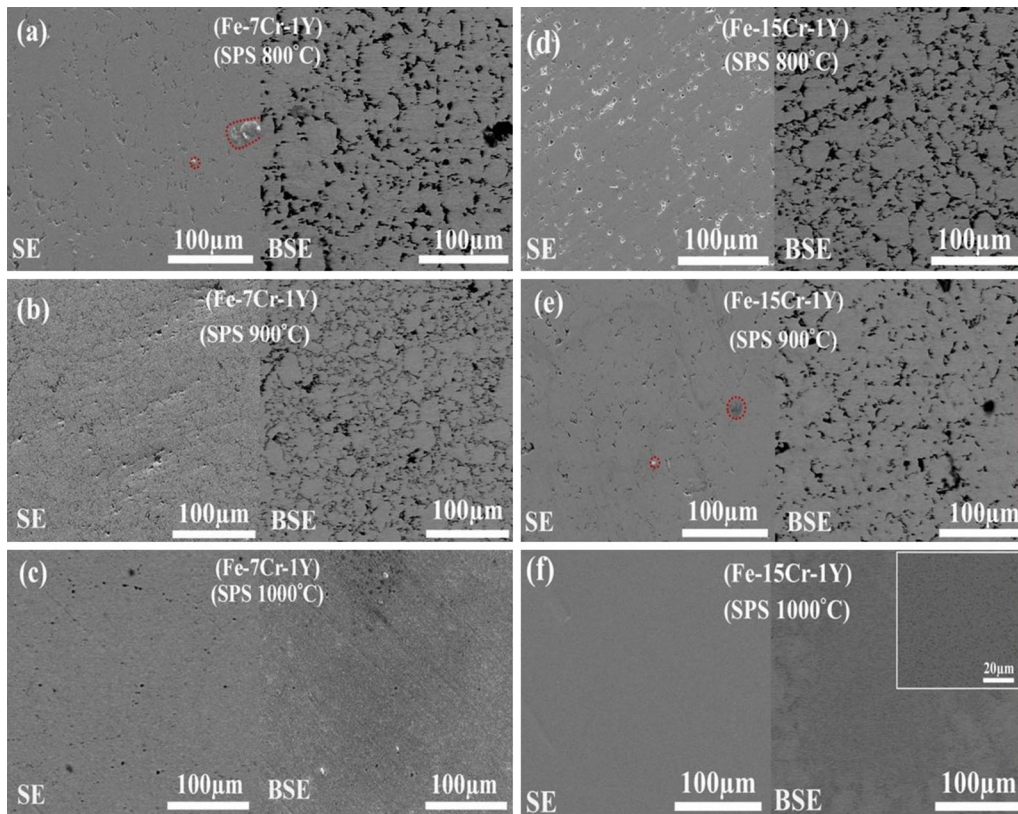


Fig. 6—FE-SEM (secondary and backscattered electron) micrographs of the bulk samples sintered at (a) 800 °C, (b) 900 °C, (c) 1000 °C for the Fe-7Cr-1Y composition; and (d) 800 °C, (e) 900 °C, (f) 1000 °C for the Fe-15Cr-1Y composition.

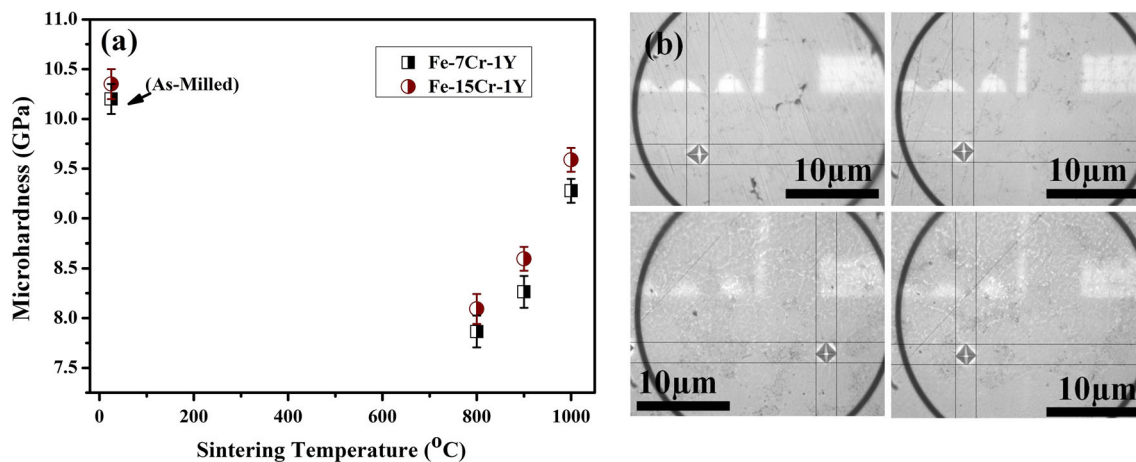


Fig. 7—(a) Variation of microhardness values as a function of sintering temperatures. (b) Showing indentation marks made within the surface during microhardness measurements.

intermetallic phase played an important role to stabilize the matrix grains in nanometer level at high temperature and also enhanced the hardness of the sintered Fe-Cr-Y alloys as discussed earlier [Figure 7(a)]. The Y atoms also played a distinguishing role in strengthening of the Cu-Y alloys as reported in Reference 45.

Figures 9(a) and (b), respectively, show the EBSD grain boundary map [high-angle grain boundaries (HABs) and low-angle grain boundaries (LABs)] and inverse pole figure of the SPSed Fe-15Cr-1Y sample

sintered at 1000 °C. According to the analyzed data shown in Figures 9(a) and (d), the major fraction of the grains is of HABs. It can be noticed that almost no black region is revealed from the EBSD image [Figure 9(b)] indicating a high sintered density of the Fe-15Cr-1Y SPSed sample (~97 pct) obtained after sintering. Figure 9(b) shows the inverse pole figure with grain boundary map of the sintered sample, which depicts a bimodal grain structures: more than 50 pct grains (in numbers) are within a range of 200 nm and remaining

grains are in the range 200 nm to 2 μm . The different grain colors indicate the orientation of each grain as shown in the inset unit triangle [Figure 9(b)]. The average grain size distribution was calculated from Figure 9(b) and is shown in Figure 9(c). Figure 9(d) shows misorientation angle of the sintered sample, which depicts that a small fraction of the grains are of LABs (up to 15 deg) and the majority is in the range of HABs with misorientation angles 15 to 60 deg. It is to be noted that the EBSD grain size distribution is corroborating well with that obtained by TEM study; both revealing a dual size grain structure (*i.e.*, up to 200 nm and 200 nm to 2 μm). Overall, the EBSD analysis shows better grain size distribution as compared to that obtained by TEM. This is due to the fact that the TEM analysis is done on extremely small sample region as compared to the sample size used for the EBSD.

B. Corrosion and Wear Behavior of the SPSed Samples

Recently, an attention has been made to replace the traditional ZG35CrMnSi steel by stabilized Fe-based alloys such as Fe-Cr-B alloys^[46] to improve the service life of the coal mining machine parts. The major part of the shearer is the sliding shoes, where the wear resistance is extremely important. A very high hardness value of the same alloy is reported in our earlier study (on thermal stability and formation kinetics of the Fe-Cr-Y alloys).^[22] In the present work also, the SPSed samples of the Fe-Cr-Y alloys show very high levels of hardness (8 to 9.5 GPa) even after SPSed at 1000 °C. Therefore, this stabilized Fe-Cr-Y alloy could be a possible candidate to replace the traditional materials such as ZG35CrMnSi steel for high wear resistance applications (*e.g.*, sliding shoes). Similarly, attention has been given to improve the properties of different parts of nuclear power plant, hot acid container, heat exchanger, petrochemical industries, and automobiles parts, where corrosion resistance is extremely vital.^[1–5] Therefore, the stabilized grade Fe-Cr-Y alloy can also be one of the possible advanced materials for the above applications, if the desired level corrosion resistance is fulfilled. Also, the role of Cr and Y could enlighten on the corrosion and wear mechanisms of SPSed Fe-Cr-Y samples, which could be useful for academic interest and other wear resistance and chemical-related applications. Therefore, the corrosion behavior and wear resistance have been discussed in the following sections.

C. Corrosion Behavior

Figures 10(a) and (b), respectively, show the potentiodynamic polarization curves as a function of current density for the Fe-7Cr-1Y and Fe-15Cr-1Y samples sintered at 800 °C, 900 °C, and 1000 °C. The potentiodynamic polarization tests were conducted at room temperature with an aerated 3.5 wt pct aqueous sodium chloride solution. The corrosion rate (CR) was determined using the following formula^[47]:

$$\text{CR (mpy)} = 0.13 \times i_{\text{corr}} (\mu\text{A}/\text{cm}^2) \times [\text{eqv. wt. of sample} / \text{density of sample}].$$

Tafel extrapolation method was used to calculate the corrosion current density (i_{corr}) and corrosion potential (E_{corr}) from the polarization curves as shown in Figure 10.

It can be noticed from Table I (as well as from Figure 10) that the corrosion resistance gradually improved with increase in the sintering temperature for both the alloys. The improvement of the corrosion resistance for the SPSed (1000 °C) sample of the Fe-15Cr-1Y alloy could be ascertained from the corresponding values of E_{corr} , i_{corr} and CR values (Table I). For the Fe-7Cr-1Y alloy sintered at 800 °C, the estimated E_{corr} , i_{corr} and CR are found to be $-0.691 \text{ V}_{\text{SCE}}$, $40.70 \mu\text{A}/\text{cm}^2$ and 18.58 mpy, respectively. Further, when the sample was sintered at 1000 °C, the corresponding values were found to be nobler [*i.e.*, $-0.590 \text{ V}_{\text{SCE}}$, $7.55 \mu\text{A}/\text{cm}^2$, and 3.46 mpy, respectively, Figure 10(a)] as compared to the sample sintered at 800 °C. The CR of the SPSed sample (sintered at 1000 °C) is quite low (only 3.43 mpy) in comparison to that (13.29 mpy) of the sample sintered at 800 °C [Figure 10(b)]. Moreover, the corrosion resistance is found to be better for the Fe-15Cr-1Y alloy as compared to that of the Fe-7Cr-1Y composition (at both the sintering temperatures). For example, the CR of the Fe-15Cr-1Y alloy sintered at 1000 °C is only 3.43 mpy as compared to 3.46 mpy for the Fe-7Cr-1Y alloy sintered at the same temperature. The improvement of the corrosion resistance can be accomplished to the improvement of the densification percentage and the presence of a large amount of noble Cr content in the Fe-15Cr-1Y alloy.

Overall, it is observed that the Fe-7Cr-1Y and Fe-15Cr-1Y alloys sintered at 1000 °C showed the maximum densification and hardness values. It clearly indicated that Fe-15Cr-1Y sample sintered at 1000 °C showed high corrosion resistance due to the presence of less porosity as compared to the other sintered samples. Guo *et al.*^[48] also observed the similar corrosion behavior for the sintered Ti-Nb₂₄-Zr₄-Sn_{7.9} samples. The sample of lower density always contains high level of interconnected porosities. When sintering temperature increase, the density also increases by eliminating the interconnected pores.^[48] Hence, there is less opportunity for the corrosive electrolyte to penetrate into the highly dense sample thereby increasing the corrosion resistance. It is known that when the porosities in the sintered samples are filled up with corrosive medium, it forms stagnation in the pores, leading to crevice corrosion.^[48] Li *et al.*^[49] investigated that in the Fe-xCr-3.5Mo-5Ni-10P-4C-4B-2.5Si alloy, an increase in the Cr content increased its thermal stability and corrosion resistance significantly. They have also explained that 4 at. pct of Cr was very effective in improving the corrosion resistance of the alloy in 3.5 wt pct NaCl solution at room temperature. Wang *et al.*^[50] reported that the addition of 2 at. pct yttrium to the bulk Fe-Cr-Mo-C-B metallic glass played an important role to have very effective corrosion resistance in 1 mol/L of HCl solution. It was explained that addition of yttrium enhanced the formation of passive films susceptibly, which improved the corrosion resistance of the bulk metallic glass.

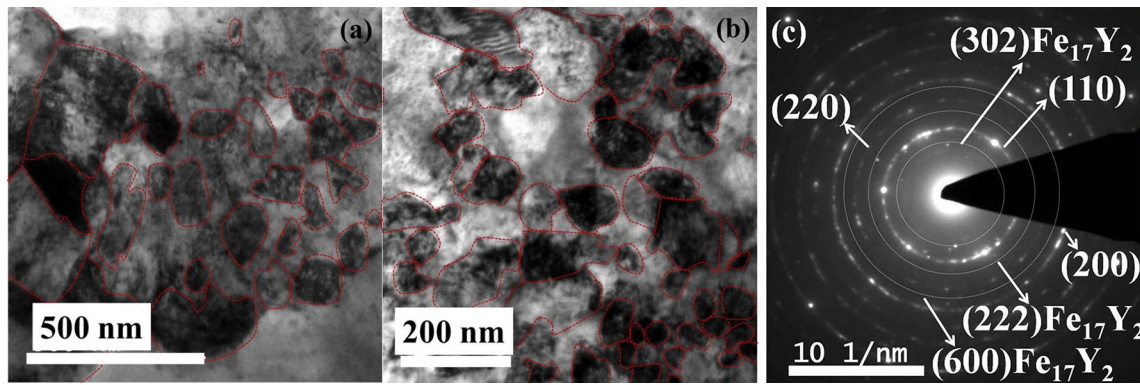


Fig. 8—Bright-field TEM images (*a* and *b*) of the Fe-15Cr-1Y SPSed at 1000 °C, (*c*) corresponding SAED pattern.

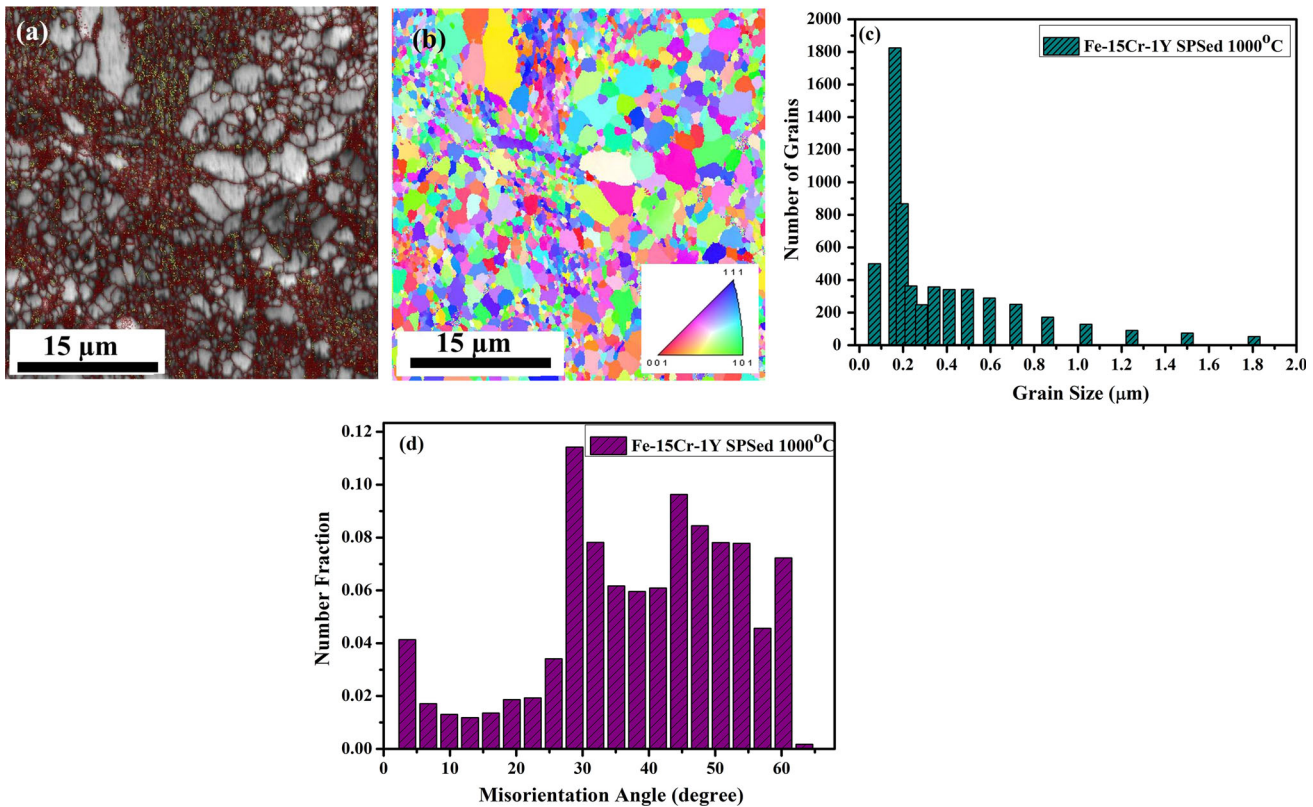


Fig. 9—EBSD images of the Fe-15Cr-1Y sample sintered at 1000 °C (*a*) grain boundary map (red lines: HABs and yellow lines: LABs), (*b*) inverse pole figure, (*c*) average grain size distribution, and (*d*) grain boundary misorientation profile (Color figure online).

Figures 11(a) through (f) show SEM images of the SPSed samples sintered at 800 °C, 900 °C, and 1000 °C after the potentiodynamic polarization test. The samples sintered at 800 °C and 900 °C [Figures 11(a) and (d)] revealed deeper pits indicating severe corrosion of the specimens. Further, the samples sintered at 1000 °C revealed very fine and shallow pits [as can be seen from Figures 11(c) and (f)] mainly because of less interconnected porosities present in the sample. Also, the specimens sintered at lower temperatures contained more open and interconnected porosities, which provided more opportunity to form deeper and larger pits.

It is also reported that high Cr content alloy leads to excellent corrosion resistance under potentiodynamic polarization test condition.^[47] It is known that when Cr alloyed with Fe changes the passivating potential of Fe to more active values and drastically lowers the critical current density required for passivation.^[47] Therefore, at very small i_{corr} values, self-passivation occurs to form an impervious passive film of Cr₂O₃, if the steel contains more than 12 pct Cr. In the present study also, the high Cr content (14.03 wt pct) alloy (*i.e.*, Fe-15Cr-1Y) showed a better corrosion resistance and less pit formation because of the formation of an impervious

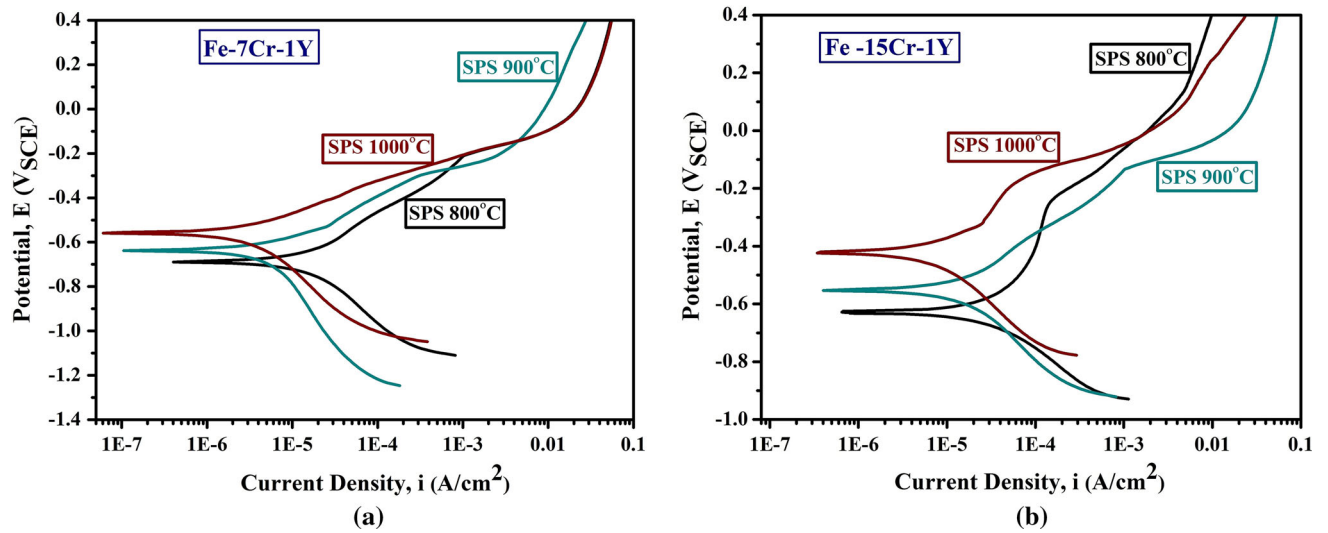


Fig. 10—Variation of potentiodynamic polarization curves as a function of current density in 3.5 wt pct NaCl solution of (a) Fe-7Cr-1Y and (b) Fe-15Cr-1Y samples sintered at various temperatures.

Table I. The Estimated Values of E_{corr} , i_{corr} , and Corrosion Rate (CR) of the Corresponding Sintered Samples are Shown

Composition	Corrosion Results ($^{\circ}\text{C}$)	E_{corr} (V _{SCE})	i_{corr} ($\mu\text{A}/\text{cm}^2$)	CR (mpy)
Fe-7Cr-1Y	800	-0.691	40.70	18.58
	900	-0.629	23.90	10.9
	1000	-0.590	7.55	3.46
Fe-15Cr-1Y	800	-0.618	29.10	13.29
	900	-0.586	14.20	8.52
	1000	-0.456	7.52	3.43

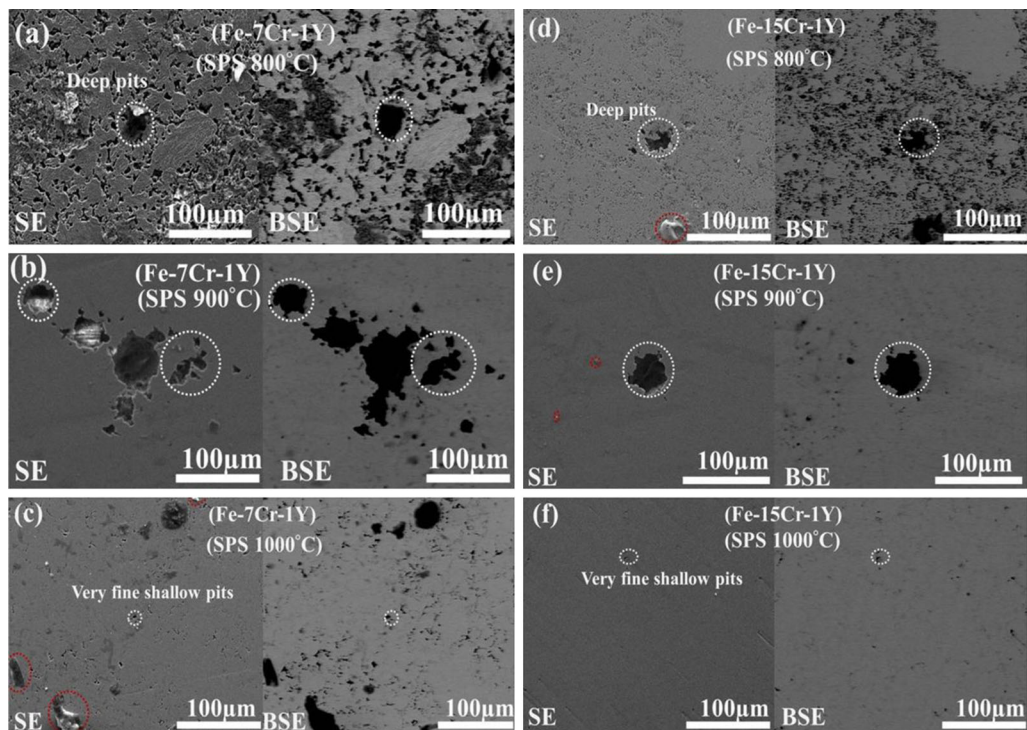


Fig. 11—FE-SEM images showing pitting surface morphology of the bulk samples sintered at (a) 800 $^{\circ}\text{C}$, (b) 900 $^{\circ}\text{C}$, (c) 1000 $^{\circ}\text{C}$ for the Fe-7Cr-1Y composition; and (d) 800 $^{\circ}\text{C}$, (e) 900 $^{\circ}\text{C}$, (f) 1000 $^{\circ}\text{C}$ for the Fe-15Cr-1Y composition.

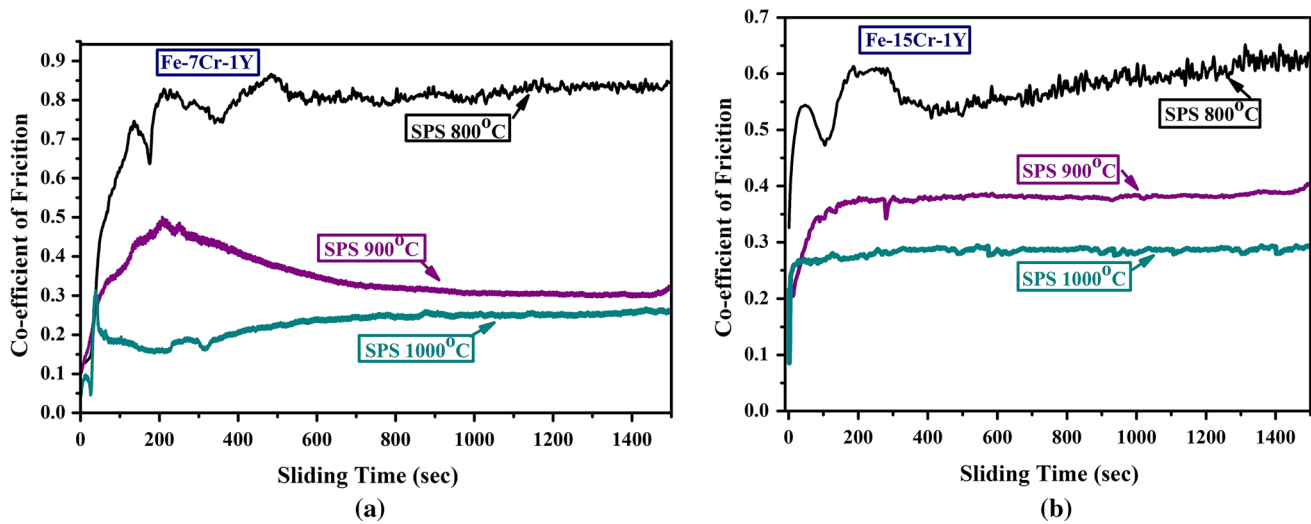


Fig. 12—Variation of coefficient of friction as a function of sliding time for the (a) Fe-7Cr-1Y and (b) Fe-15Cr-1Y alloy samples sintered at different temperatures.

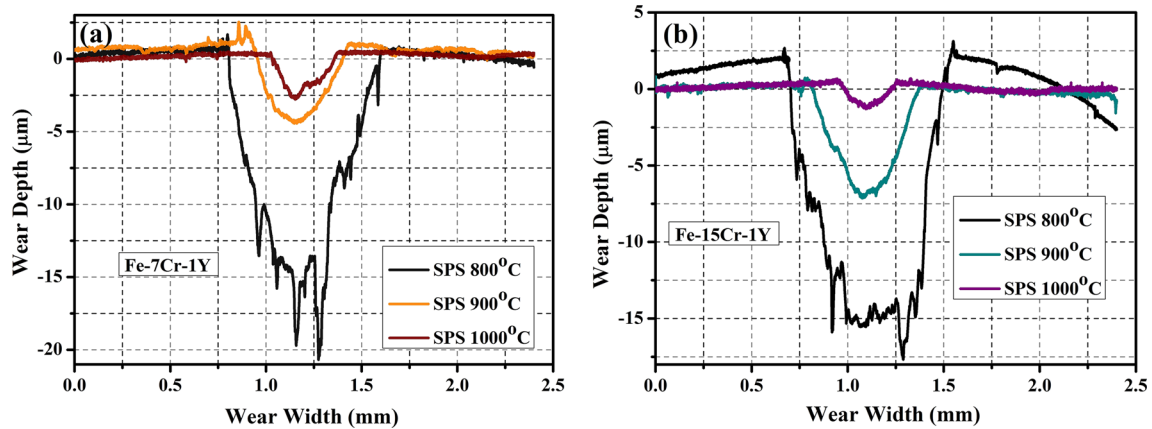


Fig. 13—Representative cross-sectional surface profiles of the worn tracks of (a) Fe-7Cr-1Y and (b) Fe-15Cr-1Y alloy samples sintered at different temperatures.

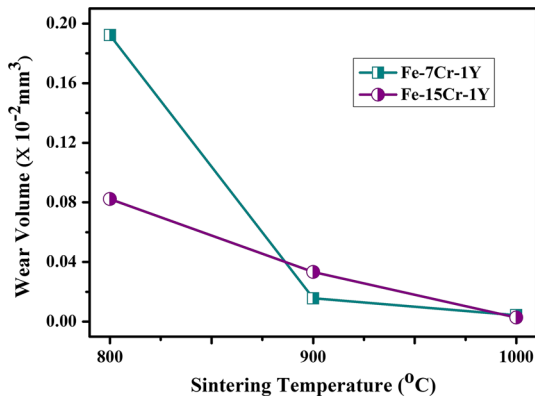


Fig. 14—Wear volumes of Fe-7Cr-1Y and Fe-15Cr-1Y sintered samples as a function of sintering temperatures.

film on the highly dense sample.^[48,49] Addition of yttrium in Fe-Cr-Mo alloy also reported to enhance the formation of passive film susceptible thereby improve the corrosion resistance.^[50]

D. Wear Properties

The dry sliding wear behavior of the SPSed Fe-7Cr-1Y and Fe-15Cr-1Y samples has been investigated and the variation of COF of the specimens as a function of time is displayed in Figure 12. As could be seen from the plots, the COF gradually decreases as the sintering temperature increased for both the alloys. As the sintering temperature increased from 800 °C to 1000 °C, the COF of the Fe-7Cr-1Y samples decreased from 0.8 to 0.3 [Figure 12(a)]. The same for the Fe-15Cr-1Y SPSed samples decreased to 0.25 from 0.6

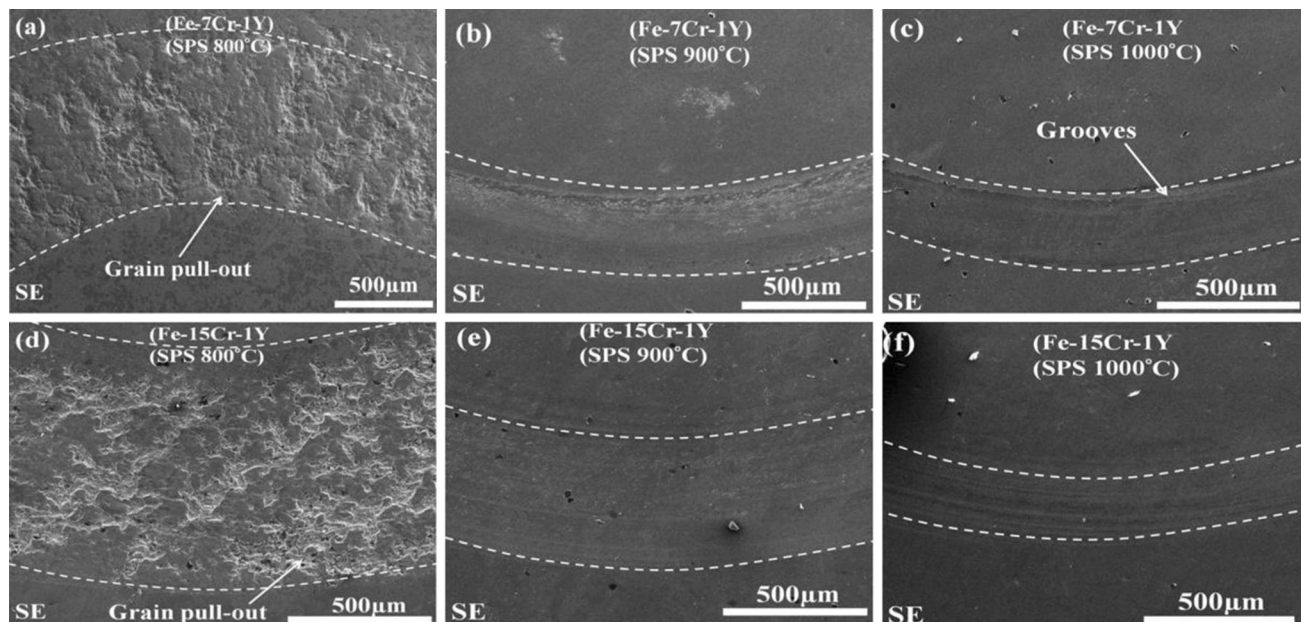


Fig. 15—FE-SEM micrographs after wear of the bulk samples sintered at (a) 800 °C, (b) 900 °C, (c) 1000 °C for the Fe-7Cr-1Y composition; and (d) 800 °C, (e) 900 °C, (f) 1000 °C for the Fe-15Cr-1Y composition.

[Figure 12(b)] as the sintering temperature increased to 1000 °C from 800 °C. Moreover, the COF of the Fe-15Cr-1Y samples is found to be less than that of the Fe-7Cr-1Y samples sintered at any particular temperature. As discussed earlier (in Figures 4 and 5), the sintered density increased with increasing sintering temperatures. The enhancement of the wear resistance, therefore, could be ascribed to the proper bonding of the powder particles and near-full density achieved during sintering at higher temperature, *i.e.*, at 1000 °C. The wear resistance was reported to improve due to the addition of 4 pct nanosize SiC particles in Cu-Cr alloys developed by MA followed by microwave sintering.^[11] Further, they also reported that at higher sintering temperature (900 °C), the wear resistance increased due to the proper bonding of the powder particles.

It can be noticed that the sample sintered at 800 °C showed more ups and downs in the COF values as compared to that of the 900 °C and 1000 °C sintered samples. This is due to the presence of more amounts of porosities and particles pull out from the surface of the low-density sample. Thus, the pull out materials (called wear debris) frequently come in contact between the ball and material surfaces, which is reflected as ups and down in the COF *vs* time plot. This, in turn, increases the formation of more amounts of wear debris particles in the low-temperature sintered sample. Li *et al.*^[51] reported similar type of results in the dry sliding wear behavior of Fe-14Mo-15Cr-2Y-15C-6B (all in at. pct) thin film metallic glass. This is an important phenomenon during the initial stage of wear, as the formation of the thin oxide layer occurs due to the oxygen-affinitive metals *viz.* iron, chromium, *etc.*, present in the alloy. Further, when this oxide layer attains certain thickness, it breaks into metal oxide debris. The

oxide debris is entrapped between the contact surface of the ball and sample, which, in turn, increases the frictional force further during sliding and induces extra wear. The wear resistance of the sintered sample is found to correlate well with the Vickers hardness values of the corresponding sample [Figure 7(a)], *i.e.*, the sample, which showed higher hardness, is less susceptible to wear. This is effective only when proper bonding between the particles is achieved and produces almost a fully dense structure. Many other researchers also reported that the highly dense Fe-based alloys having high Cr and Y showed excellent tribological performance and wear resistance.^[11,52,53] The Cr and Y elements played a vital role to improve the wear resistance and decreased the COF.^[52,53]

Figures 13(a) and (b), respectively, show the cross-sectional surface profiles of the worn tracks of the sintered Fe-7Cr-1Y and Fe-15Cr-1Y samples. Both, the depth and width of the sliding wear tracks were measured at different locations by using surface profilometer. Figures 13(a) and (b) clearly indicate that the wear depth and wear width values are larger for the samples, which were sintered at lower temperature (*e.g.*, Fe-7Cr-1Y: 17.5 μm and 0.79 mm and Fe-15Cr-1Y: 15 μm and 0.94 mm for 800 °C sintered sample). The worn depth and width of the same samples decreased to only 2.5 μm and 0.35 mm and 1.5 μm and 0.25 mm, respectively, as the sintering temperature increased to 1000 °C. At the beginning, the wear width and depth increased very rapidly due to the initial loading effect and the presence of porosities. This effect is more prevalent for the low-density samples as large amounts of loosely bound particles are pulled out from the surface. Therefore, more wear debris would be accumulated on the surface of the low-density samples.

On the basis of the surface profile analysis, the wear volume was calculated using Archard's formula^[52] as follows:

$$\text{Wear volume (mm}^3\text{)} = 2\pi \times \text{track radius} \times \text{track width} \times \text{wear depth.}$$

Figure 14 demonstrates the wear volume of the sintered samples as a function of sintering temperature. It can be noted that the wear volume decreased with increase in the sintering temperatures for both the alloys. For the samples sintered at 800 °C, the wear volume is estimated to be 0.01922 and $0.0823 \times 10^{-2} \text{ mm}^3$, respectively, for the low and high Cr content alloys. The wear volume decreased to only 0.00439 and $0.00277 \times 10^{-2} \text{ mm}^3$, respectively, when the sintering was carried out at 1000 °C. As mentioned earlier, the wear resistance increased due to the increase in the relative sintered density and formation of proper bonding between the particles. Also, the Cr and Y played a vital role to improve the wear resistance due to their solid solution strengthening and precipitation hardening effect.^[53,54]

To correlate the COF and surface profile after the wear test, the wear track surface of the corresponding sintered sample was analyzed from their FE-SEM images. Figures 15(a) through (f) show the wear track surfaces of the samples sintered at different temperatures. It can be noticed from Figures 15(a) and (d) that the wear track surfaces were much wider and a large amount of material wore out from the surface of the low-temperature (800 °C) sintered samples of the Fe-7Cr-1Y and Fe-15Cr-1Y alloys. A large number of particles are found to pull out from both the surfaces because of improper bonding of the powder particles.

On the other hand, the wear track width was found to gradually narrow down (indicating better wear resistance) as the sintering temperature increased. The minimum wear track width is achieved for the high Cr content Fe-15Cr-1Y alloy sintered at 1000 °C [Figure 15(f)]. The wear track width is found to be highly consistent with the COF and worn depth and width of the corresponding sample. Cui *et al.*^[53] also reported that addition of Cr in Cu-Pb alloy strengthened the matrix and improved the wear resistance. Addition of 2 wt pct Y in a cobalt-base alloy (stellite-6) was reported to increase its wear resistance at room temperature as well as elevated temperatures due to the increased strengthening effect of Y.^[54] They also reported that the worn surface of the Y-free sample showed larger wear track as compared to that of the 2 wt pct Y alloy.^[54]

IV. CONCLUSIONS

Bulk size nanocrystalline Fe-7Cr-1Y and Fe-15Cr-1Y alloy samples have been synthesized successfully by MA followed by SPS. The SPS process has been optimized to obtain near-full density bulk samples, which show high

wear resistance and hardness and improved corrosion resistance. In this regard, the following outcomes could be concluded from the study.

- (i) The maximum densification of 97 pct was achieved for the Fe-15Cr-1Y alloy when sintered at 1000 °C. The high level of sintered density is ascribed to the prevalent grain boundary diffusion at higher sintering temperature and formation of necks due to the deformation at contact points (because of applied pressure).
- (ii) The TEM and EBSD analysis confirmed that the grain size of the sintered sample depicts a bimodal grain structures: more than 50 pct grains are within a range of 200 nm and remaining grains are in the range 200 nm to 2 μm . The EBSD grain size corroborated well with the TEM grain size.
- (iii) The Vickers hardness values were found to be quite high (9.27 and 9.58 GPa for the Fe-7Cr-1Y and Fe-15Cr-1Y samples, respectively) even after sintering at 1000 °C. The wear rate of the Fe-15Cr-1Y SPSed sample was estimated to be very low, which was confirmed from the wear volume ($0.00277 \times 10^{-2} \text{ mm}^3$) analysis and COF (2.5) of the corresponding sample. The wear resistance was found to consistent well with the SEM images of the worn surface.
- (iv) The corrosion resistance of the highly dense Fe-15Cr-1Y sample (sintered at 1000 °C) was detected to improve (CR = 3.43 mpy) as compared to that of the other sintered samples (13.29 mpy). The SEM images of the corroded samples also confirmed the same.

ACKNOWLEDGMENTS

The authors highly acknowledge the Department of Metallurgical and Materials Engineering and Institute Instrumentation Centre, IIT Roorkee for providing the facilities and support to carry out the research work.

REFERENCES

1. N.R. Baddoo: *J. Constr. Steel Res.*, 2008, vol. 64, pp. 1199–206.
2. K. Oha, S. Ohnuki, S. Yamashita, N. Akasaka, S. Ohtsuka, and H. Tanigawa: *Mater. Trans.*, 2007, vol. 48, pp. 2563–66.
3. D. Peckner and I.M. Bernstein: *Handbook of Stainless Steel*, 2nd ed., McGraw Hill Book Company, New York, 1977, pp. 160–65.
4. A.A. Sorour, H.W. Strauss, R.R. Chromik, and M. Broch: *Tribol. Lett.*, 2011, vol. 44, pp. 269–78.
5. R. Gupta, R.K. Singh Raman, and C.C. Koch: *Mater. Sci. Eng. A*, 2008, vol. 494, pp. 253–56.
6. G.E. Dieter: *Mechanical Metallurgy*, 2nd ed., McGraw Hill Book Company, New York, 1961, pp. 120–42.
7. M. Meyers, A. Mishra, and D. Benson: *Prog. Mater. Sci.*, 2006, vol. 51, pp. 427–556.
8. R. Valiev, R. Islamgaliev, and I. Alexandrov: *Prog. Mater. Sci.*, 2000, vol. 45, pp. 103–89.
9. Z.A. Munir, U. Anselmi-Tamburini, and M. Ohyanagi: *J. Mater. Sci.*, 2006, vol. 41, pp. 763–77.

10. C. Suryanarayana: *Prog. Mater. Sci.*, 2011, vol. 46, pp. 1–84.
11. S. Mula, P. Sahani, S.K. Pratihari, S. Mal, and C.C. Koch: *Mater. Sci. Eng. A*, 2011, vol. 528, pp. 4348–56.
12. A.J. Song, M.Z. Ma, R.Z. Zhou, L. Wang, W.G. Zhang, and C.L. Tan: *Mater. Sci. Eng. A*, 2012, vol. 538, pp. 219–23.
13. T. Sasaki, T. Ohkubo, and K. Hono: *Acta Mater.*, 2009, vol. 573, pp. 3529–38.
14. S. Libardi, M. Zadra, F. Casari, and A. Molinari: *Mater. Sci. Eng. A*, 2008, vol. 478, pp. 243–50.
15. I. Toor, J. Ahmed, M.A. Hussein, and N. Al-Aqeeli: *Powder Technol.*, 2016, vol. 299, pp. 62–70.
16. J.R. Groza: in *Nanostructured Materials*, C.C. Koch, ed., Noyes Publications, William Andrew Publishers, New York, 2002, pp. 115–78.
17. R.W. Siegel: *Mater. Sci. Forum*, 1997, vol. 238, pp. 851–85.
18. M.B. Shongwe, S. Diouf, M.O. Durowoju, and P.A. Olubambi: *J. Alloys Compd.*, 2015, vol. 649, pp. 824–32.
19. D. Sebayang, D.S. Khaerudini, H. Saryanto, M.A. Othman, M. Husin Saleh, D. Fredrick, and P. Untoro: *Appl. Mech. Mater.*, 2011, vol. 54, pp. 2197–2202.
20. C. Suryanarayana and M.G. Norton: *X-Ray Diffraction*, 1st ed., Plenum Publishing Corporation, New York, 1998.
21. B.D. Cullity and S.R. Stock: *Elements of X-ray Diffraction*, 3rd ed., Prentice Hall, London, 2001.
22. V.M.S. Muthaiah, L.H. Babu, C.C. Koch, and S. Mula: *Mater. Charact.*, 2016, vol. 114, pp. 43–53.
23. M. Saber, W. Xu, L. Li, Y. Zhu, C.C. Koch, and R.O. Scattergood: *J. Nucl. Mater.*, 2014, vol. 452, pp. 223–29.
24. W.Z. Xu, L.L. Li, M. Saber, C.C. Koch, Y.T. Zhu, and R.O. Scattergood: *Metall. Mater. Trans. A*, 2015, vol. 46A, pp. 4394–4404.
25. W.Z. Xu, L.L. Li, M. Saber, C.C. Koch, Y.T. Zhu, and R.O. Scattergood: *J. Nucl. Mater.*, 2014, vol. 452, pp. 434–39.
26. J. Saenko: *Phase Equilib. Diffus.*, 2017, vol. 38, pp. 684–99.
27. M. Mihalkovic and M. Widom: *Phys. Rev. B*, 2004, vol. 70, p. 144107.
28. K. Mandal, A. Yan, P. Kersch, A. Handstein, O. Gutfleisch, and K.H. Muller: *J. Phys. D*, 2004, vol. 37, pp. 2628–31.
29. S.B. Rybalka: *Mater. Lett.*, 2015, vol. 5, pp. 437–41.
30. S. Pasebani and I. Charit: *J. Alloys Compd.*, 2014, vol. 599, pp. 206–11.
31. J.H. Schneibel and S. Shim: *Mater. Sci. Eng. A*, 2008, vol. 488, pp. 134–38.
32. K.A. Darling, B.K. VanLeeuwen, J.E. Semones, C.C. Koch, R.O. Scattergood, L.J. Kecskes, and S.N. Mathaudhu: *Mater. Sci. Eng. A*, 2011, vol. 528, pp. 4365–71.
33. M. Saber, H. Kotan, C.C. Koch, and R.O. Scattergood: *Mater. Sci. Eng. A*, 2012, vol. 556, pp. 664–70.
34. L. Li, M. Saber, W. Xu, Y. Zhu, C.C. Koch, and R.O. Scattergood: *Mater. Sci. Eng. A*, 2014, vol. 613, pp. 289–95.
35. S. Mula, S. Ghosh, and S.K. Pabi: *Powder Technol.*, 2009, vol. 191, pp. 176–81.
36. A.P. Kumar, V.M.S. Muthaiah, and S. Mula: *J. Alloys Compd.*, 2017, vol. 722, pp. 617–27.
37. V. Mamedov: *Powder Metall.*, 2002, vol. 45, pp. 322–28.
38. T.J. Goodwin, S.H. Yoo, P. Matteazzi, and J.R. Groza: *Nanostruct. Mater.*, 1997, vol. 8, pp. 559–66.
39. M. Omori: *Mater. Sci. Eng. A*, 2000, vol. 287, pp. 183–88.
40. G.E. Fougere, J.R. Weertman, and R.W. Siegel: *Nanostruct. Mater.*, 1995, vol. 5, pp. 127–34.
41. R.S. Averback, H. Zhu, R. Tao, H.J. Hofler, and D.L. Bourell: *Synthesis and Processing of Nanocrystalline Powder*, TMS, Warrendale, PA, 1996, pp. 203–16.
42. H. Zhu and R.S. Averback: *Mater. Manuf. Process.*, 2007, vol. 11, pp. 905–23.
43. H.W. Zhang, R. Gopalan, T. Mukai, and K. Hono: *Scripta Mater.*, 2005, vol. 53, pp. 863–68.
44. M.A. Hussein, C. Suryanarayana, A.M. Kumar, and N. Al-Aqeeli: *Mater. Des.*, 2015, vol. 83, pp. 344–51.
45. S. Mula, D. Setman, K. Youssef, R.O. Scattergood, and C.C. Koch: *J. Alloys Compd.*, 2015, vol. 627, pp. 108–16.
46. H. Xuan and G. Cui: *Ind. Lubr. Tribol.*, 2017, vol. 69, pp. 142–48.
47. M.G. Fontena: *Corrosion Engineering*, 3rd ed., Tata McGraw-Hill Edition, New York, 2005.
48. S. Guo, A. Chu, H. Wu, C. Cai, and X. Qu: *J. Alloys Compd.*, 2014, vol. 597, pp. 211–16.
49. J. Li, L. Yang, H. Ma, K. Jiang, C. Chang, J.Q. Wang, Z. Song, X. Wang, and R.W. Li: *Mater. Des.*, 2016, vol. 95, pp. 225–30.
50. Z.M. Wang, Y.T. Ma, J. Zhang, W.L. Hou, X.C. Chang, and J.Q. Wang: *Electrochim. Acta*, 2008, vol. 54, pp. 261–69.
51. Z. Li, C. Zhang, and L. Liu: *J. Alloys Compd.*, 2015, vol. 650, pp. 127–35.
52. J.F. Archard: *J. Appl. Phys.*, 1953, vol. 24, pp. 981–88.
53. H. Cui, J. Guo, Y. Su, H. Ding, W. Bi, X. Li, and H. Fu: *Mater. Sci. Eng. A*, 2007, vol. 448, pp. 49–55.
54. L. Wang and D.Y. Li: *Wear*, 2003, vol. 255, pp. 535–44.